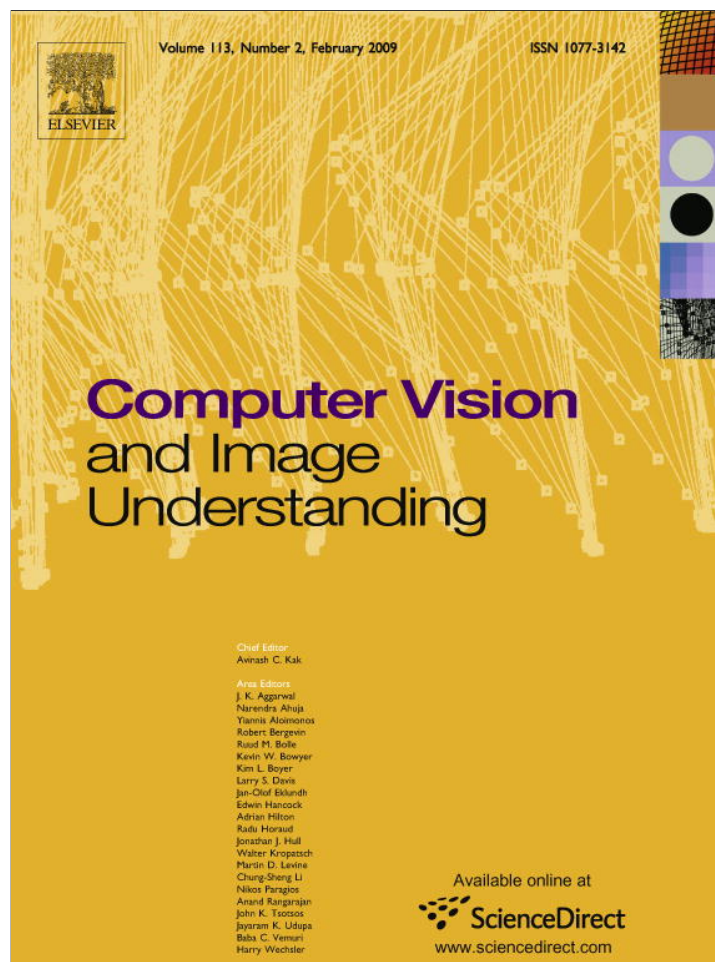


Provided for non-commercial research and education use.  
Not for reproduction, distribution or commercial use.



This article appeared in a journal published by Elsevier. The attached copy is furnished to the author for internal non-commercial research and education use, including for instruction at the authors institution and sharing with colleagues.

Other uses, including reproduction and distribution, or selling or licensing copies, or posting to personal, institutional or third party websites are prohibited.

In most cases authors are permitted to post their version of the article (e.g. in Word or Tex form) to their personal website or institutional repository. Authors requiring further information regarding Elsevier's archiving and manuscript policies are encouraged to visit:

<http://www.elsevier.com/copyright>



Contents lists available at ScienceDirect

# Computer Vision and Image Understanding

journal homepage: [www.elsevier.com/locate/cviu](http://www.elsevier.com/locate/cviu)

## Morphological multiscale decomposition of connected regions with emphasis on cell clusters

Oliver Schmitt<sup>a,\*</sup>, Maria Hasse<sup>b</sup><sup>a</sup> Institute of Anatomy, University of Rostock, Gertrudenstrasse 9, D-18055 Rostock, Germany<sup>b</sup> Institute of Mathematics University of Rostock, Universitätsplatz 1, D-18051 Rostock, Germany

### ARTICLE INFO

#### Article history:

Received 20 January 2007

Accepted 15 August 2008

Available online 11 September 2008

#### Keywords:

Image analysis  
Multiscale morphology  
Decomposition  
Separation  
Subdivision  
Splitting  
Partitioning  
Decoupling  
Cell clustering  
Cell grouping

### ABSTRACT

After binarization of cells in complex cytological and histological images the segmented structures can be rather far away from a final quantification of features of single cells since cells may overlap and cluster strongly. Separating optically, partially or totally fused entities like cells is a problem which frequently cannot be solved by a watershed segmentation or a basic morphological processing of images. However, considering different morphological scales after iterative erosion gives rise to dominant markers of singular objects. Performing a reconstruction by iterative dilation yields a scale-independent decomposition of multiple disjointed cell clumps of different sizes within an image.

Accordingly we developed a technique that splits cell clumps into meaningful parts. Since this method is based on the analysis of the morphological-scale space, generated by iterative erosion, it is independent on the size of cell clusters. The detection of dominant points within the eroded scales are cell-specific markers. The converse integration of markers at different scales is obtained by a successive reconstruction based on constrained dilation of the original cell shape.

The advantages of this approach are the independence of cell shapes which are clumped, the consideration of holes or background intensities within objects and the robustness with regard to convergence. An important benefit is the fitting of the operation time to the size of clusters by the size of the morphological structuring element. This means, that this approach requires only one parameter. Finally, a better match of the morphological scale space approach was found and compared with the ground truth as well as the results of the watershed technique.

The primary object of this paper is to highlight the algorithm and its results by using different examples from benchmark databases, self generated images that exhibit different topological features and complex configurations of cells within histological images.

© 2008 Elsevier Inc. All rights reserved.

### 1. Introduction

Image analytic-based cell measurements in diascopic micrographs of stained cells in histological sections depend strongly on staining features, local cell distributions and variability of their size and shape [100]. The section thickness leads to considerable differences of gray-level or color distributions within cells. In the case of sections of the central nervous system stained with cresyl violet thicker sections of 10–20  $\mu\text{m}$  give rise to almost dark stained neurons whereby thin sections of about 5  $\mu\text{m}$  yields a pale nucleus, a dark nucleolus and a definable perikaryon. These features that influence the complexity of a digitized histological scene are also true for other organs. In this contribution, we focus on cell aggregations in the central nervous system and address several exam-

ples of further objects in images that can be split by the same approach presented. Many areas within the brain of vertebrates exhibit dense neuron distributions which even persist in thin sections where partial or total overlaps of structures in consequence of optical projection appear. Likewise, optical fusion appears if cells are juxtaposed very closely like the small granular cells of the cerebellum or those in the dentate gyrus.

To summarize, micrographs of stained histological sections of the brain will probably contain overlaps of structures, due to distribution, when projecting a 3D-physical structure into a 2D-image.

These overlaps are reduced in confocal laser scanning microscopy (CLSM) [1,3]. However, for long-term measurements of large areas of histological sections, for instance serial sections of brains, CLSM is inapplicable and motorized video microscopy [102] or high-resolution transparent flat bed scanning [101] need to be performed.

Cytological as well as histological analysis of cell parameters [139,91,19,86,62,30] assume that the objects to be measured, i.e.

\* Corresponding author. Fax: +49 381 494 8402.

E-mail addresses: [schmitt@med.uni-rostock.de](mailto:schmitt@med.uni-rostock.de) (O. Schmitt), [maria.hasse@uni-rostock.de](mailto:maria.hasse@uni-rostock.de) (M. Hasse).

cell bodies and/or cell nuclei are not connected. Reliable automatic processing of cytological and histological digital images is particularly demanded for clinical routine purposes as well as for basic science. Naive methods like conditioned and scale space-based erosion [131] result in an unsatisfying splitting if objects are juxtaposed very closely. Even sophisticated procedures like watershed segmentation of heavily clustered cells with different shape and size may fail [125,9,124,63,75,23,20,122,2,52,27].

For many years [80,37,39,85,94,105,114,111,135] much effort has been spent to decompose such cell overlaps (for an overview see e.g. [8]) as the successful splitting of these cells is the key to automatic quantitative cell analysis in cytology and histology [64]. However, for extensive overlaps of hundreds or thousands of structures in images where the area of the foreground is larger than the background (Figs. 1a" and 4g) the decomposition problem becomes complex. Automatic morphometry [6] of complex cell dis-

tributions in histological sections of biological material is a challenging task in combination with registration of serial sections [73] in order to generate complete cell atlases of organs, especially brains [61]. This cutting-edge technology most often uses mice as species for genetic modifications. These are knocking out or knocking in of specific genes inducing different kinds of effects like morphological changes especially of the brain that must be recognized, analyzed and compared quantitatively at the cellular level.

The problem of touching objects [4] persists after image analytic processes (denoising, shading correction, normalization) are applied. In many cases these preprocessing steps are followed by global segmentation using standard methods [112,138,79,96,40,128] that produce bilevel, resp. half-tone images that contain sufficient foreground information for further cell-object specific processing. Classical techniques like Hough-transform are useful if particles possess regular shapes (circles or ellipses) [50]. The structural anal-

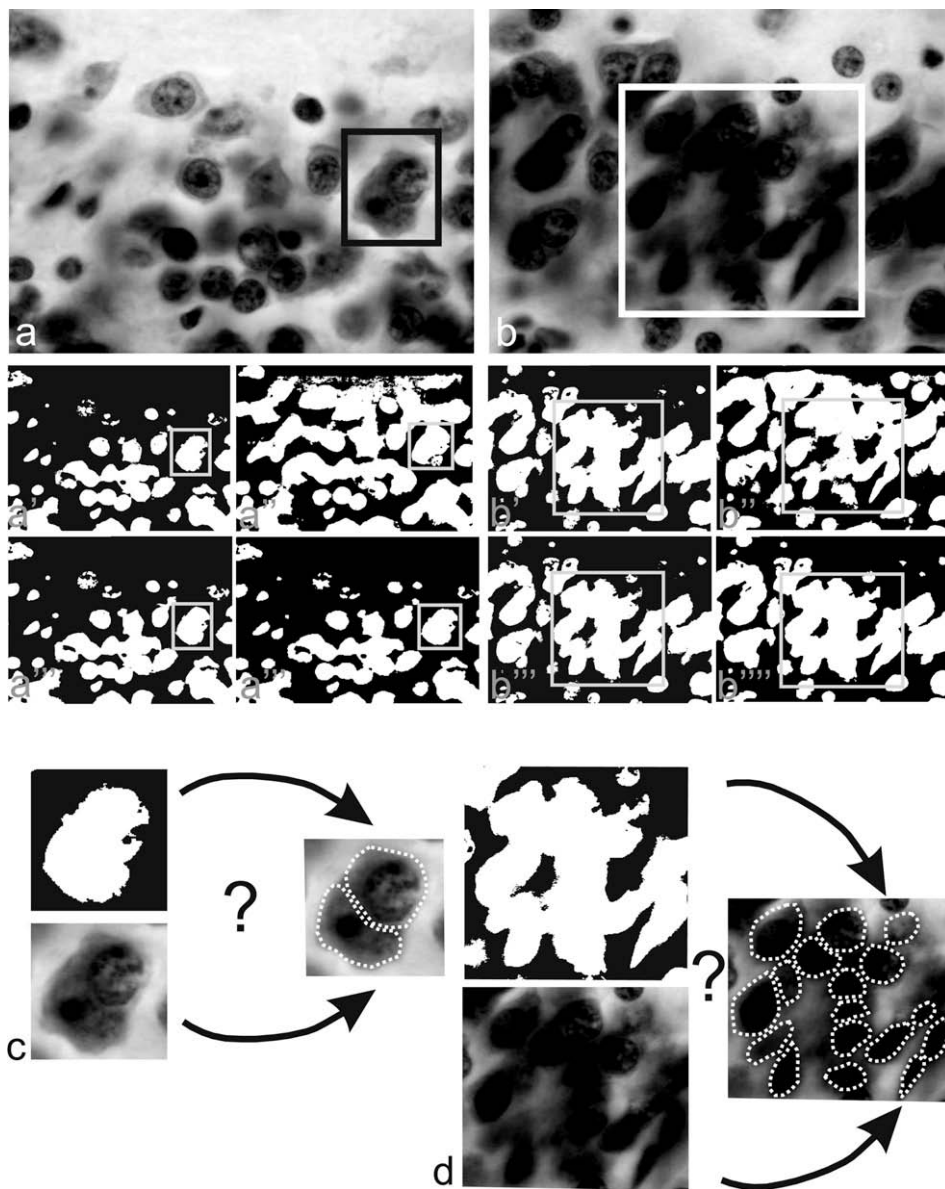


**Fig. 1.** The decomposition problem and differences of binarization of cell images. (a) First sample image with a superposition of two disjoint nerve cells (rectangle). (b) Second sample image with a strong spatial clustering of cells (rectangle). (a') Global segmentation with the Otsu-method. (a'') Local adaptive segmentation. (a''') K-means segmentation. (a''') Mean-shift segmentation (same as in b'-b'''). Binarizations are comparable: the segmentation results lead to strongly fused cell objects. (c) Superimposed gray scaled and binarized cells for which a decomposition should be found. At least the cell boundary should be reconstructed used for masking and further operations. (d) Clustered gray scaled and binarized cells for which a decomposition should be found and cell boundaries should be reconstructed.

ysis of cytological images is often performed by means of morphological filter [127,28,87,71] because of their shape-, rather than frequency-orientated operations [67]. Such nonlinear approaches are well suited for shape description [41] and decomposition [66,88]. The concept of morphological operations has been extended to multiscale shape representations [98,121,46,38]. By applying morphological multiscale decomposition (MSD)[42] an image containing fused regions is decomposed into size-specific scales, each

carrying markers representing disjoint regions. The detected markers are used to reconstruct successively original shapes without fusing them again. This kind of morphology based separation can be adapted to different shapes of aggregated particles as shown by [113,71]. Aggregates that consist of particles of certain sizes can be segmented by appropriate morphological processing whereas the shape and size of cells in biological specimens may vary considerably (Fig. 1c and d).

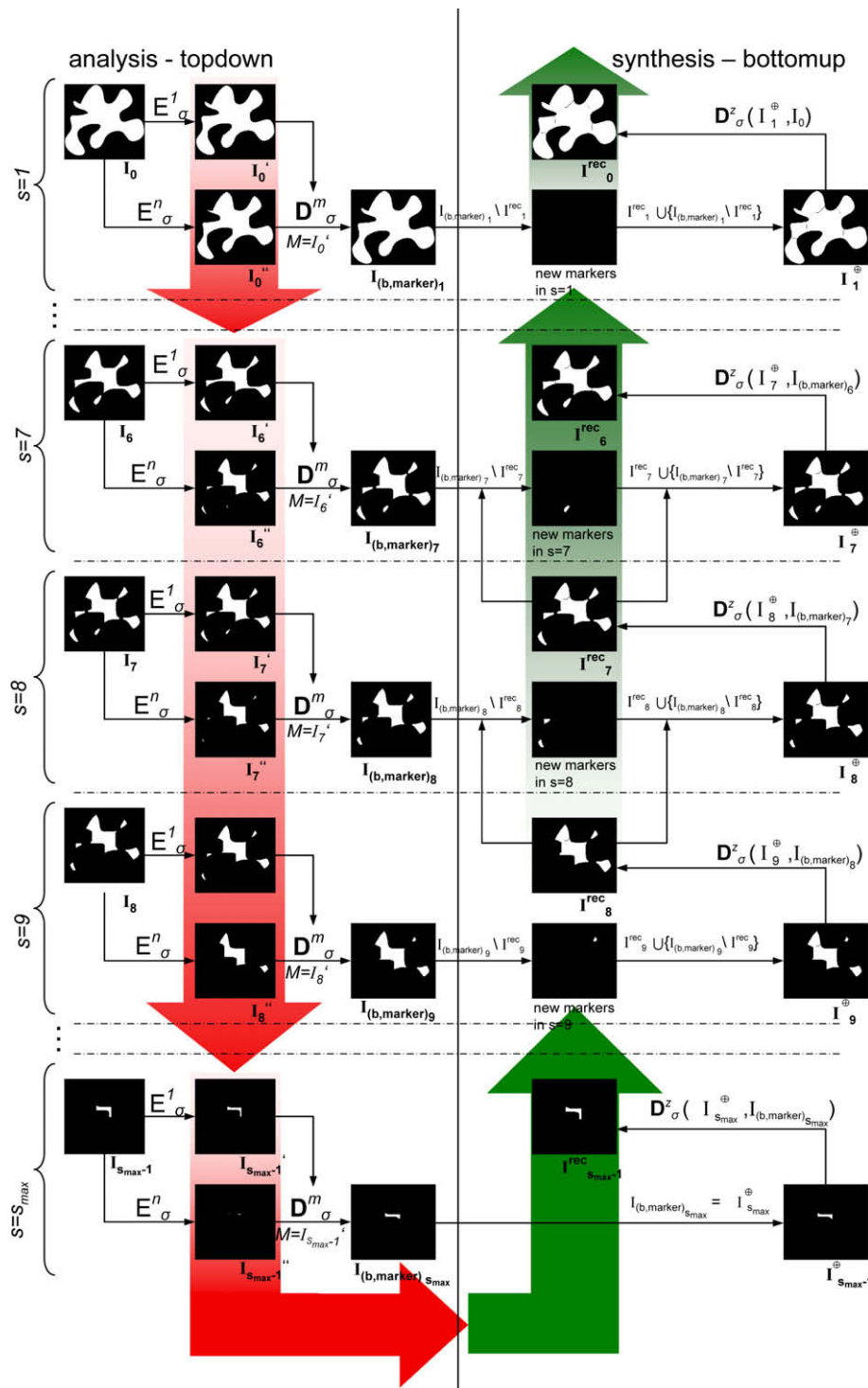


Fig. 2. Illustration of the steps of the algorithm. On the left the topdown and on the right the bottomup processing is shown.  $E$  is an erosion and  $D$  a dilation. Disjoint markers of the cells are separated by the two steps of erosion and dilation, respectively, opening (topdown). After reaching the steady state of the analysis process the synthesis by merging and reconstruction is performed to reach the original cell shapes in image  $I_0^{\oplus}$ . At the same time the separate markers are prevented and splitting is secured.

Aggregates may appear as two touching cells or large clusters with many holes, i.e. connected regions of background within an aggregate (Fig. 1a and b). Contour-based algorithms are used for such complex clusters. Mostly, these algorithms determine centroids of decomposed particles followed by a precise gray scale-based segmentation by the watershed method or region growing. Contour-based algorithms determine dominant points, i.e. concavities and convexities of the contour and test which cut path or split path of opposite dominant points turns out to minimize a cost function. Further methods aim to separate by applying active contours and level sets. A comprehensive overview of recent literature concerning these families of aggregate-particle-problems and algorithms is given in the following:

- *Morphology-based procedures*: [12,119,55–57,125,8,75,70,74,23],
- *Contour-based techniques*: [68,22,116,134,11,113,53,99,107,51,93,48,126],
- *Active contour-based methods*: [16,140,104,6],
- *Graph theoretic approaches* [36,35],
- *Parametric fitting algorithms* [24,113,133,130] and
- *Level set approach* [24,103].

So far, a comprehensive benchmark using a database of cell clumps or clumped objects is not available. In this article we compared the splitting results of the most often applied watershed method with the multiscale-based morphological algorithm described in Section 2.2.

The linear concept of multiscale-based filtering was introduced in terms of a systematic application to image analysis by [14,129]. Later on, this approach was applied to shape-based decomposition through morphological filters [45,120,97,38] and optimized for efficient subdivision problems in image analysis [13,47,98,132,46,71]. Subdivision by morphological multiscale processing was applied successfully to split touching objects in images generated from projections of fibroblasts in cytological micrographs [71].

In this contribution, we have implemented the algorithm and solved different problems that arose within testing the modified method on test images of differing topological features. Virtues and limitations of the morphological multiscale decomposition (MSD) technique are explicated and compared with the standard approach of watershed-based decomposition (WSD). Our investigations have shown promising results when applying this splitting method to complex cell clusters obtained from different digitizing techniques, like bright field microscopy and high-resolution transparent flat bed scanning [101].

The objective of this study is to decompose cell agglomerates to localize cell borders (Fig. 1c and d). Based on the localization of cell borders in the form of closed polygons (Fig. 1c and d) the regions can be masked and intensity distributions of localized cells can be analyzed. The result of the splitting of systematic modified test images and real biological images was compared with images in which an expected partition was defined by an investigator to allow comparisons of the splitting outcomes.

## 2. Materials and methods

For the realization, testing and modification of the morphological multiscale method (MSD) we used three families of images: synthetic images (*arte*) (Fig. 3), light microscopic images of cell clusters (*cells*) (Fig. 4a) [101] and high-resolution transparent flat bed scanned images [100] of histological sections of mouse brains stained with the modified method of Gallyas (*scan*) [33,101] (Figs. 4d–f and 8c–u). In comparison to typical shapes of a cluster, one of the synthetic images (Fig. 3d) was systematically modified (Fig. 3f–k) by inserting combinations of holes within the object to study the effects on the splitting results. In Fig. 3b and c, as well as in Fig. 4i

and j, corners appear in combination with concavities and convexities. Such contour features of these synthetic test images are comparable with some regions of contours of cell clusters that are composed of pyramidal neurons, multipolar neurons or endothelial cells. In Fig. 8 many segments of the contours possess a corner like appearance due to the optical resolution of transparent flat bed scans. With regard to space limitation we have chosen typical and complex biological examples from a collection of biological test images with a sample size of 10,000 which are also used for artificial network training to classify cell objects [89].

Each digital image  $f$  is a function  $f : (i, j) \rightarrow l_{ij}$  that maps discrete coordinates to a finite range of a matrix  $I$  of the size  $m$ -by- $n$ ,  $I = (l_{ij})_{i,j=1}^{m,n}$ , whereas  $I$  is either denoted as  $I_{(g)}$  with gray-values or levels  $l_{ij} \in \{0, \dots, 255\}$  or as  $I_{(b)}$  with two-levels, resp. binary values  $l_{ij} \in \{0, 1\}$ .

Gray-level images were segmented by the global segmentation method of [78] (Fig. 1) followed by an opening and closing to remove oversegmented small regions and fill undersegmented small holes. Opening and closing were performed applying a symmetric diamond shaped structuring element of size 3. By closing an image, the filling of small holes will effect the splitting result, because they do not contribute any more to the formation of evolving markers within the multiscale morphological procedure as well as to disturbances in the distance transform for the watershed procedure. Because cells are the objects of interest, the opening deletes small foreground objects which do not belong to the compartment of cell bodies. Therefore, oversegmentation will be reduced.

We decided to apply the segmentation of [78] after testing further techniques (local adaptive, K-means, mean-shift). The outcomes of these segmentation algorithms are shown in Fig. 1a and b. The results of the Otsu, K-means [69,15,54] and mean-shift [33,17,18] segmentations are quite similar. The local adaptive segmentation provides better segmentations for small disjoint cells whereby noise (Fig. 1a and a") appears in the binarized image and regions of fused cells are obviously larger. Many further promising segmentation methods are possible to apply, e.g. texture-based [49], adaptive fuzzy c-means methods [82–84,81] or gradient vector fields [136,137], however, after finding similar results of different global thresholding methods, the more complex techniques were not tested.

Binarization gives rise to connected components due to juxtaposed objects of interest. Therefore, images are divided in foreground and background. We define the sets  $X^1 \subseteq I_{(b)}$  and  $X^0 \subseteq I_{(b)}$  with

$$X^1 = \{(i, j); l_{ij} = 1\} \rightarrow \text{foreground} \quad (1)$$

$$X^0 = \{(i, j); l_{ij} = 0\} \rightarrow \text{background} \quad (2)$$

Now we state  $X^1 \cup X^0 = I_{(b)}$ . The subset  $X_i^1 \subseteq X^1$  is a *connected component* or *object* if the points  $x \in X_i^1$  of the image  $f$  are neighbored with regard to a given metric so that they can be labeled commonly by a certain attribute. The foreground is the union of connected components  $X^1 = \bigcup_i X_i^1$ .

Connected components can be decomposed by the conventional *watershed transformation* [91,64] that is a matter of common knowledge realized by an efficient pixel list sorting algorithm [122]. Therefore, the algorithm of the watershed decomposition (WSD) is not explained. Regarding the digital topology, 8-connectivity was used. The Euclidean distance was applied to calculate distance maps of binary images. We used the WSD to compare its results with the approaches developed here. There exist four basic preprocessing steps for applying the WSD: (1) directly smoothing the gray-level image, (2) distance transformation of a binary segmented image, (3) marker-based WSD (seeded watershed) and (4) internal and external regions approach [64]. Here, the dis-

tance transformation of binary segmented images was used. Finally, the distance transformed images were smoothed by a  $5 \times 5$  median filter because small concavities and convexities of the contours cause numerous small peaks in the distance transform landscape. If the distance transform is not smoothed a strong oversegmentation will appear. It turns out that a  $5 \times 5$  filter size is optimal for the negative effects in distance transforms caused by roughness of the contours. However, the filter size must be adjusted with regard to single object size, cluster size and roughness of the contours of clusters. In Section 3 the splitting result of the WSD will be presented first, followed by the results of the morphological multiscale decomposition. As both algorithms decompose the same pre-processed (noise reduced) binary image it is indicated that a positive comparison has been made.

### 2.1. Expected decomposition (EXD)

The human decomposed images provide ground truth boundaries and are designated as *expected decompositions* (EXD). The EXDs contain boundaries marked by human subjects that are considered to be valid. However, sometimes multiple segmentations (*multiple ground truth*) of an image by different subjects exist. This is largely due to image segmentation and object splitting being ill-defined problems. In these cases the most common manual-marked boundary was considered as the *singular ground truth* in a set of acceptable solutions. All EXDs have been hand-labeled by experts in neurohistology to obtain a unique set of splittings for comparison with the algorithm results. These splittings are made on principles of Gestalt theory [25]. Due to these principles [29,7,10,76,60,44,109] components of objects are analyzed by investigators [43]. Information along visual contours that is relevant for cognitive subdividing of objects is concentrated in regions of high magnitude of curvature [5], rather than being distributed uniformly along the contour. [5] indicates that most shape information is contained in the corners (high curvature points), which allows to characterize the contour. This has been investigated more precisely by [29] in regard to information theory [89,108]. Based on the Gestalt principles *proximity, similarity, continuity, and closure* of human perception, experts were instructed to concentrate on sharp inflections possessing a topological relation in order to outline the expected split paths [115]. In the EXD images of Fig. 4a', c'-f the locations of cells are marked by circles. This labeling can be compared easily with the results of the WSD and MSD splittings in Fig. 7.

### 2.2. Morphological multiscale decomposition (MSD)

The constitution of cells in brain tissue is rather variable with regard to the size and shape of cells. Therefore, a multiscale approach appears to be appropriate in order to decompose cell clusters which are composed of highly variable cells.

The morphological multiscale decomposition is generated by operators that employ scalable templates by using a morphological structuring element  $\sigma$ . The scaling number  $s$  determines the grade of the generated level. Using a morphological operator  $\mathcal{M}$  that transforms the image  $f$ , we note a scale of  $s$  levels as the following:

$$\mathcal{M}_{\sigma^0}(f) := f \quad (3)$$

$$\mathcal{M}_{\sigma^1}(f) := \mathcal{M}_{\sigma}(f) \quad (4)$$

$$\mathcal{M}_{\sigma^s}(f) := \mathcal{M}_{\sigma^s}^s(f) \quad (5)$$

Images generated by a scalable operator  $\mathcal{M}$  at a certain scale are noted as:

$$F_s := \mathcal{M}_{\sigma^s}(f) \quad \text{with} \quad F_0 = f$$

The scale space  $F : \mathbb{N} \times \mathbb{X}^{m \times n} \rightarrow \mathbb{B}$  needs the scale number  $s$  with  $s \in \mathbb{N}$ .

In a first step, the image is decomposed into size-specific scales of distinct morphological markers  $I_{(b, \text{marker})_s}$ , each of them indicate a disjoint cell without dealing with its shape. The converse synthesis of scales reconstructs the cell size and cell shape but prevents the merging of already separated regions. The benefit of this approach is a scale-independent decomposition, because differently sized cells are treated within their proper scale.

Morphological reconstruction filters are dual filters that consist of  $n$ -fold erosion  $\mathcal{E}_{\sigma}^n(I_{(b)})$  and  $n$ -fold dilation  $\mathcal{D}_{\sigma}^n(I_{(b)})$  [106,110,26]. Eroded and dilated images contain the markers of the binary image  $I_{(b)}$  of disjoint regions. These markers are determined by applying a circular binary structuring element of radius  $\sigma$ . To store the marker pixels a binary masking image  $M_{(b)}$  is applied within a  $n$ -fold masked erosion  $\mathcal{E}_{\sigma}^n(I_{(b)}, M_{(b)})$  and dilation  $\mathcal{D}_{\sigma}^n(I_{(b)}, M_{(b)})$ . The masked operator gives rise to a white-reconstruction  $\mathcal{R}_{\sigma}^{\infty}(I_{(b)}, M_{(b)})$ . The reconstruction was realized by iterating a masked morphological operation until  $B$  reaches a steady state as denoted by  $\infty$ .

The reconstruction of level  $s + 1$  is performed with the binary masking image  $M_{(b)} = I_{(b, \text{marker})_{s+1}}$  ( $M_{(b)}$ : the masking image) by expanding the initially smaller objects of  $I_{(b, \text{marker})_s}$ . However, we need a process to prohibit merging of expanding marker regions. By using the dual operator white-skiz  $\mathcal{Z}_{\sigma}^z(I_{(b)}, M_{(b)})$  ( $z$ : skeleton-by-influence-zone (skiz)) expanding marker regions do not merge [72]. Basically, the white-skiz is the skeleton of the background and an analog to the watershed transform of graylevel images [106,77]. A one-pixel gap between those objects of  $I_{(b)}$  that are covered by markers in  $M_{(b)}$  will appear. Hence, the number of regions in  $\mathcal{Z}_{\sigma}^z(I_{(b)}, M_{(b)})$  equals those in  $M_{(b)}$ .

The  $n$ -fold opening  $\mathcal{O}_{\sigma}^n(I_{(b)}) := \mathcal{D}_{\sigma}^n(\mathcal{E}_{\sigma}^n(I_{(b)}))$  and closing  $\mathcal{C}_{\sigma}^n(I_{(b)}) := \mathcal{E}_{\sigma}^n(\mathcal{D}_{\sigma}^n(I_{(b)}))$  are ordered sequences of dilation and erosion. The reconstructive opening and closing take the steady states into account [21]:

- $n$ -fold opening by reconstruction:

$$\mathcal{O}_{\sigma}^{(n, \infty)}(I_{(b)}, M_{(b)}) := \mathcal{D}_{\sigma}^n(\mathcal{E}_{\sigma}^n(I_{(b)}), M_{(b)}) \quad (6)$$

- $n$ -fold closing by reconstruction:

$$\mathcal{C}_{\sigma}^{(n, \infty)}(I_{(b)}, M_{(b)}) := \mathcal{E}_{\sigma}^n(\mathcal{D}_{\sigma}^n(I_{(b)}), M_{(b)}) \quad (7)$$

This binary processing represent a reconstruction of  $I_{(b)}$  from  $M_{(b)}$  after noise filtering by an appropriate dual filter to suppress non-relevant markers due to noise. The noise emerges from the process of optoelectronic imaging and from biological small structures that do not belong to the structures of interest, e.g. cells. In the case of  $M_{(b)} = I_{(b)}$  the  $n$ -fold opening and closing by reconstruction filters give rise to a nonlinear noise reduction by concomitantly preserving boundaries of regions by removing compartments smaller than the  $n$ -fold iterated operator  $\sigma$ . Finally, the  $n$ -fold opening and closing by reconstruction processes can be combined by their successive application. This leads to the  $n$ -double reconstruction filter:

$$\Psi_{\sigma}^{(n, \infty)}(I_{(b)}) := \mathcal{C}_{\sigma}^{(n, \infty)}(\mathcal{O}_{\sigma}^{(n, \infty)}(I_{(b)}, I_{(b)}), I_{(b)}) \quad (8)$$

This filter removes white and black regions from  $I_{(b)}$  that do not belong to compartments of interest (cells and cell clusters). Here, we applied a double reconstruction filter of size  $\sigma = 1$  whereby  $\sigma$  is the radius of the symmetric  $3 \times 3$  structure element which turns out to be well below the expected minimal area of small glial cells and small neurons like granular cells.

We hypothesize that decomposition of binary regions composed of connected cells can be separated best by using distinct markers within their size-specific scale. Individual cells can be seg-

mented progressively by reconstructing them from their markers determined by an iterative erosion process until reaching a steady state. First, the markers are derived in a *topdown* procedure realized by enhanced erosion that starts at the noise filtered binary image (*top*) and erodes regions *down* to their marker(s). Furthermore, the topdown procedure analyzes enhanced erosion results. Each erosion step  $s$  produces a marker scale  $I_{(b,\text{marker})_s}$ . At least, this yields one distinct marker for each cell. The following *bottomup* procedure makes use of enhanced dilation to reconstruct the original shapes, while preventing already separated markers from merging again.

The analytical topdown procedure starts at the binary image  $I_{(b)}$  that represents the markers at scale  $0 \leq s \leq k \in \mathbb{N}$ , where  $k$  is the total number of scales. The complete scale-space is generated by a sequence of  $k$  successive enhanced erosions, respectively, constrained openings:

$$I_{(b,\text{marker})_s} = \mathcal{D}_\sigma^m \left[ \underbrace{\mathcal{E}_\sigma^n(I_{(b,\text{marker})_{s-1}})}_{I_{(b,\text{marker})_{s-1}}^{\text{erodn}}}, \underbrace{\mathcal{E}_\sigma^1(I_{(b,\text{marker})_{s-1}})}_{I_{(b,\text{marker})_{s-1}}^{\text{ero1}}} \right] \quad (9)$$

where  $\mathcal{D}_\sigma^m$  and  $\mathcal{E}_\sigma^n$  denote  $m$ -fold dilation and  $n$ -fold erosion. At the scale  $s$ , the  $n$ -eroded marker image  $\mathcal{E}_\sigma^n(I_{(b,\text{marker})_{s-1}})$ , respectively,  $I_{(b,\text{marker})_{s-1}}^{\text{erodn}}$  is  $m$ -fold dilated by the condition of an 1-fold erosion  $\mathcal{E}_\sigma^1(I_{(b,\text{marker})_{s-1}})$  which is underbraced and denoted as  $I_{(b,\text{marker})_{s-1}}^{\text{ero1}}$  leading to the next scale image  $I_{(b,\text{marker})_s}$ . Each of these scale images initialize subdivisions of those cells belonging to that specific scale. In such a way the markers  $X_i^1 \subseteq I_{(b,\text{marker})_{s-1}}$  represent those objects that are larger than  $\sigma^{ns}$ :

$$\forall X_i^1 \subseteq I_{(b,\text{marker})_{s-1}} \exists X_j^1 \subseteq I_{(b)} : \#(X_j^1 \subseteq I_{(b)}) > \sigma^{ns}$$

The parameters  $n$  and  $m$  are derived from *a priori* knowledge of the smallest biological object of the specimen under investigation. The erosion  $\mathcal{E}_\sigma^n(I_{(b,\text{marker})_{s-1}})$  with  $n=3$  removes all objects  $\#(X_i^1 \subseteq I_{(b,\text{marker})_{s-1}}) > \sigma^{ns}$  which size corresponds to the scale  $s$ . As well as initial  $n$ -double reconstruction, the  $n$ -fold erosion filters false markers and for this  $n=3$  is appropriate for all scales. If connected components consist of subregions  $\#(X_i^1 \subseteq I_{(b,\text{marker})_{s-1}})$  having strong shape variations the erosion  $\mathcal{E}_\sigma^n(I_{(b,\text{marker})_{s-1}})$  may filter multiple disjoint markers  $X_{j_1}^1 \subseteq I_{(b,\text{marker})_s}$  with  $X_{j_1}^1 \cap X_{j_2}^1 \cap \dots = \emptyset$  and  $X_{j_1}^1 \subseteq I_{(b,\text{marker})_s} \subset X_i^1 \subseteq I_{(b,\text{marker})_{s-1}}$ .

Since Eq. 9 actually represents an opening,  $m \leq n$  is a side condition for the  $m$ -fold dilation. For  $m=n$  the number of false markers is too large and yields a trade-off of reducing markers and decomposition of connect components sizes. However, a  $m$ -fold dilation by  $m=n+1$  gives rise to satisfying (see Section 3) subdivisions of cell clusters. The total number of scales  $k$  is an uncritical parameter since it is above a certain threshold that depends on the maximum size of cells. Because we applied the procedure to images of different kinds of clusters covering variable shapes and sizes of objects it turned out to be optimal to perform ultimate stepping through the morphological scale space (MSS). The pseudocode of the topdown procedure is given in Algorithm 1.

The marker scales  $I_{(b,\text{marker})_s}$  are processed by enhanced dilations to recover original cell regions in  $I_{(b)}$  that should be separated. For each image at scale  $s$  an image  $I_{(b)}^{\text{rec}}$  is reconstructed (Fig. 2). The reconstructed image  $I_{(b)}^{\text{rec}}$  incorporates the information of all those markers of scale  $\geq s$  and preserves their subdivided regions. The markers are reconstructed to the original size of objects of scale  $s$  by combining  $I_{(b)}^{\text{rec}}$  and  $I_{(b,\text{marker})_s}$ , whereas  $I_{(b,\text{marker})_s} \supseteq I_{(b)}^{\text{rec}}$ . Hence, the resulting image  $I_{(b)}^{\text{rec}}$  consists of all markers of  $I_{(b)}^{\text{rec}}$  and those contained in  $I_{(b,\text{marker})_s}$ , but not in  $I_{(b)}^{\text{rec}}$ :

$$I_{(b)}^{\text{rec}} = I_{(b)}^{\text{rec}} \cup \left\{ I_{(b,\text{marker})_s} \setminus I_{(b)}^{\text{rec}} \right\} \quad (10)$$

The latter step ensures that no subdivision is lost during reconstruction. The pseudocode of the bottomup procedure is given in Algorithm 2. At last, a white-skiz reconstruction is applied to extend the shapes of  $I_{(b)}^{\text{rec}}$  to those of  $I_{(b,\text{marker})_s}$  preserving their partitions. Then we obtain the reconstructed markers  $I_{(b)}^{\text{rec}}$  of scale  $s$ , whereas  $I_{(b,\text{marker})_{s-1}}$  is used as a mask:

$$I_{(b)}^{\text{rec}} = \mathcal{D}_\sigma^z \left( I_{(b)}^{\text{rec}}, I_{(b,\text{marker})_{s-1}} \right). \quad (11)$$

Additionally to the pseudocode that will be presented next, the steps of the MSD approach are visualized to show the differences of intermediate data at different scales in Fig. 2.

#### Algorithm 1. Topdown

**Require:** originalImage,  $\sigma$ .

**Ensure:**  $I_{(b,\text{marker})_s}, S = 1, \dots, k$ .

```

1:  $I_{(b,1)} = \text{originalImage}$ 
2:  $s = 0$ 
3:  $n = 3$ 
4:  $m = n + 1$ 
5: while  $\Sigma\Sigma(I_{(b,1)}) > 0$  do
6:    $s = s + 1$ 
7:    $I_{(b,2)} = \mathcal{E}_\sigma(I_{(b,1)})$  {1-fold erosion of  $I_{s-1}$ ;  $I_{(b,2)} = \mathcal{E}_\sigma^1(I_{s-1})$ }
8:    $I_{(b,3)} = I_{(b,2)}$ 
9:   for  $i = 2$  to  $n$  do
10:     $I_{(b,3)} = \mathcal{E}_\sigma(I_{(b,3)})$  { $n$ -fold erosion of  $I_{s-1}$ ;  $I_{(b,3)} = \mathcal{E}_\sigma^n(I_{s-1})$ }
11:   end for
12:    $I_{(b,4)} = I_{(b,3)}$ 
13:   for  $i = 1$  to  $m$  do
14:     $I_{(b,4)} = \mathcal{D}_\sigma(I_{(b,4)})$  { $m$ -fold dilation of  $I_{(b,3)}$ ;  $I_{(b,4)} = \mathcal{D}_\sigma^m(I_{(b,3)})$ }
15:    {with  $I_{(b,2)} = \mathcal{E}_\sigma^1(I_{s-1})$  as masking image}
16:    for all  $I_{(b,4)}$  such that  $I_{(b,4)} > I_{(b,2)}$  do
17:       $I_{(b,4)} = 0$ 
18:    end for
19:    $I_{(b,\text{marker})_s} = I_{(b,4)}$ 
20:    $I_{(b,1)} = I_{(b,4)}$ 
21: end while
22:  $k = s$  { $k = \text{total number of scales}$ }
```

#### Algorithm 2. Bottomup

**Require:** originalImage,  $\sigma, I_{(b,\text{marker})_s}, S = k, \dots, 0$ .

**Ensure**  $I_{(b,\text{rec})}$ .

```

1:  $I_{(b,1)} = \text{originalImage}$ 
2:  $I_{(b,2)} = I_{(b,\text{marker})_{k-1}}$ 
3:  $I_{(b,\text{rec})} = I_{(b,\text{marker})_{k-1}}$ 
4:  $I_{(b,\text{recGap})} = I_{(b,\text{marker})_{k-1}}$ 
5: for  $s = k - 2$  downto 0 by step  $-1$  do
6:   if  $s = 0$  then
7:      $I_{(b,3)} = I_{(b,1)}$ 
8:   else
9:      $I_{(b,3)} = I_{(b,\text{marker})_{s-1}}$  {mask for  $\mathcal{D}_\sigma^z$  in line 17}
10:  end if
11:   $I_{(b,4)} = I_{(b,\text{rec})} + (I_{(b,2)} - I_{(b,\text{recGap})})$  {creating  $I_{(b,4)} = I_s^{\text{rec}}$ }
12:  for all  $I_{(b,4)}$  such that  $I_{(b,4)} == 2$  do
13:     $I_{(b,4)} = 0$  {revision of modification from line 34}
14:  end for
15:  while TRUE do
16:     $I_{(b,\text{pb})} = I_{(b,4)}$ 
17:     $I_{(b,4)} = \mathcal{D}_\sigma(I_{(b,4)})$  {dilation  $\mathcal{D}_\sigma^z(I_s^{\text{rec}})$ }
18:    {with  $I_{(b,3)} = I_{(b,\text{marker})_{s-1}}$  as masking image}
19:    for all  $I_{(b,4)}$  such that  $I_{(b,4)} > I_{(b,3)}$  do
```

```

19:  $I_{(b,4)} = 0$ 
20: end for
    {skeleton of background to prevent merging}
21:  $objBorders = skiz(abs(1 - I_{(b,pb)}))$ 
22:  $I_{(b,4)} = I_{(b,4)} + ((-2) \cdot objBorders)$ 
23:  $[xgap, ygap] = find(I_{(b,4)} == -1)$ 
24:  $I_{(b,4)}(find(I_{(b,4)} == -1)) = 0$ 
25:  $I_{(b,4)}(find(I_{(b,4)} == -2)) = 0$ 
26:  $I_{(b,pa)} = I_{(b,4)}$ 
27: if  $I_{(b,pb)} = I_{(b,pa)} I_{(b,4)}$  reached a steady state
28:    $I_{(b,rec)} = I_{(b,4)}$ 
29:    $I_{(b,recGap)} = I_{(b,4)}$ 
30:   if  $length(xgap)$  then
31:     for  $k = 1$  to  $length(xgap)$  do
32:       {modifying  $I_{(b,rec)}$  in order to prevent gaps from
        disappearing in line 11}
33:        $I_{(b,recGap)}(xgap_k, ygap_k) = -1$ 
34:     end for
35:   end if
36:   break {leaving while-loop because  $I_{(b,4)}$  reached a steady
    state}
37: end if
38: end while
39:  $I_{(b,2)} = I_{(b,3)}$ 
40: end for
    
```

### 3. Results

In the following the results of the morphological multiscale decomposition (MSD) and the watershed-based decomposition (WSD) in consideration of the expected decompositions (EXD) are presented.

#### 3.1. Expected decompositions (EXD)

These partitions are shown in Figs. 3 and 4. Different persons have partitioned the objects or separated images of cell clusters as shown in Fig. 4. These images are considered as optimal partitions which are compared to the results obtained by MSD and WSD.

#### 3.2. Watershed-based decomposition (WSD)

The WSD leads to satisfying results if regions of a connected component do not exhibit too strong overlaps Figs. 5a2, b2, d2 and 6a2–g2. However, small subregions positioned around a relative large area Fig. 5e2 and small protrusions with corners Fig. 5f2 produce considerable differences in comparison to EXDs. The WSD result of the circle cluster Fig. 5g2 yields an optimal splitting with regard to EXD. Regarding the more complex clusters in Fig. 7b2 we obtain comparable results as observed before. Oversegmentations occur more frequently than undersegmentations. At different regions we find cap-like oversegmentations. Larger objects exhibiting small concavities on their contours are undersegmented. The binary image of cells in Fig. 7c2 shows rather more undersegmentations. In the scanned mouse brain three cell clusters were isolated and analyzed separately. In Fig. 7d2 the upper part of the cluster was splitted better than by the MSD method. However, the lower part of this cluster was oversegmented. The cluster in Fig. 7e2 shows an undersegmentation at the upper right part which was splitted correctly by the MSD method. Additionally, in this cluster an oversegmentation is produced by the WSD whereas Fig. 7f2 shows a satisfying result, however, some parts of the cluster are still undersegmented.

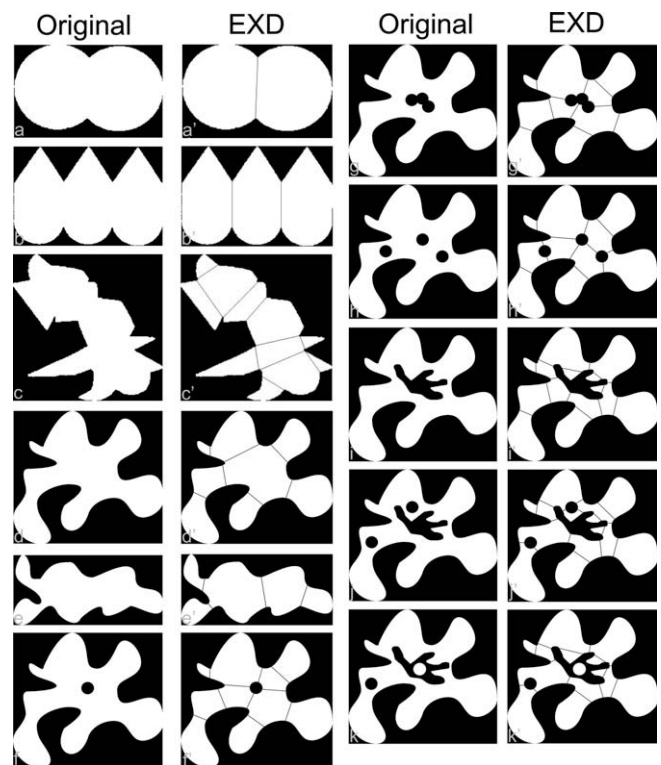


Fig. 3. Synthetic images used for developing and testing the decomposition algorithms. Letters without apostrophe designate the original images and those with an apostrophe the expected decompositions done by investigators. (a–c) IPAN test images ([http://visual.ipan.szaki.hu/corner/corner\\_click.html](http://visual.ipan.szaki.hu/corner/corner_click.html)), [59]. In contrast to the IPAN test images we used test images with different kind of holes and regions within holes.

#### 3.3. Morphological multiscale decomposition (MSD)

The MSD was applied to the same images like EXD and WSD. Marginal undersegmentations are found in example Fig. 5c1, e1 and f1 whereas the latter shows more splitted parts than the result of WSD. However, in the case of Fig. 5c1 the two determined split paths fit slightly better to the EXD results in Fig. 5c3 than those of the WSD results in Fig. 5c2. The cluster of circles in Fig. 5g1 was decomposed nearly complete.

Applying the MSD to synthetic images with connected domains (holes) (Fig. 6) a remarkable influence of determining split paths can be observed. The elongated image Fig. 6a1 are similar to the WSD result of Fig. 6a2. In Fig. 6b1 one short split of a small protrusion is missing, but all other separations are optimal in comparison to the EXD image (Fig. 6b3). In Fig. 6c1 we can observe an important effect of MSD which consists in generating split paths from convexities of holes to concavities of the cluster contours. This can be observed also in Fig. 6d1, e1, f1 and g1. Split paths were generated between holes of the connected domain as shown in Fig. 6e1 but not between convexities of the same connected domain. In Fig. 6f1 and g1 a connected domain of circular shape is located between three adjacent concavities of the surrounding contour. To each of three concavities split paths were constructed.

The more complex examples in Fig. 7 show different results of decomposition for MSD and WSD. In these images mixtures of small and large cell clusters as well as non-clustered cells occur. In Fig. 7a1 MSD detected slightly less objects but produced fewer oversegmentations than WSD. This phenomenon can be observed in Fig. 7b1 and c1, too. The decomposition by MSD of neuron clusters of the mouse brain (Fig. 7d1, e1, and f1) show less oversegmentations than those of the WSD (Fig. 7d2, e2, and f2) and in Fig. 7e1 a correct additional splitting that is absent in the WSD result (Fig. 7e2).

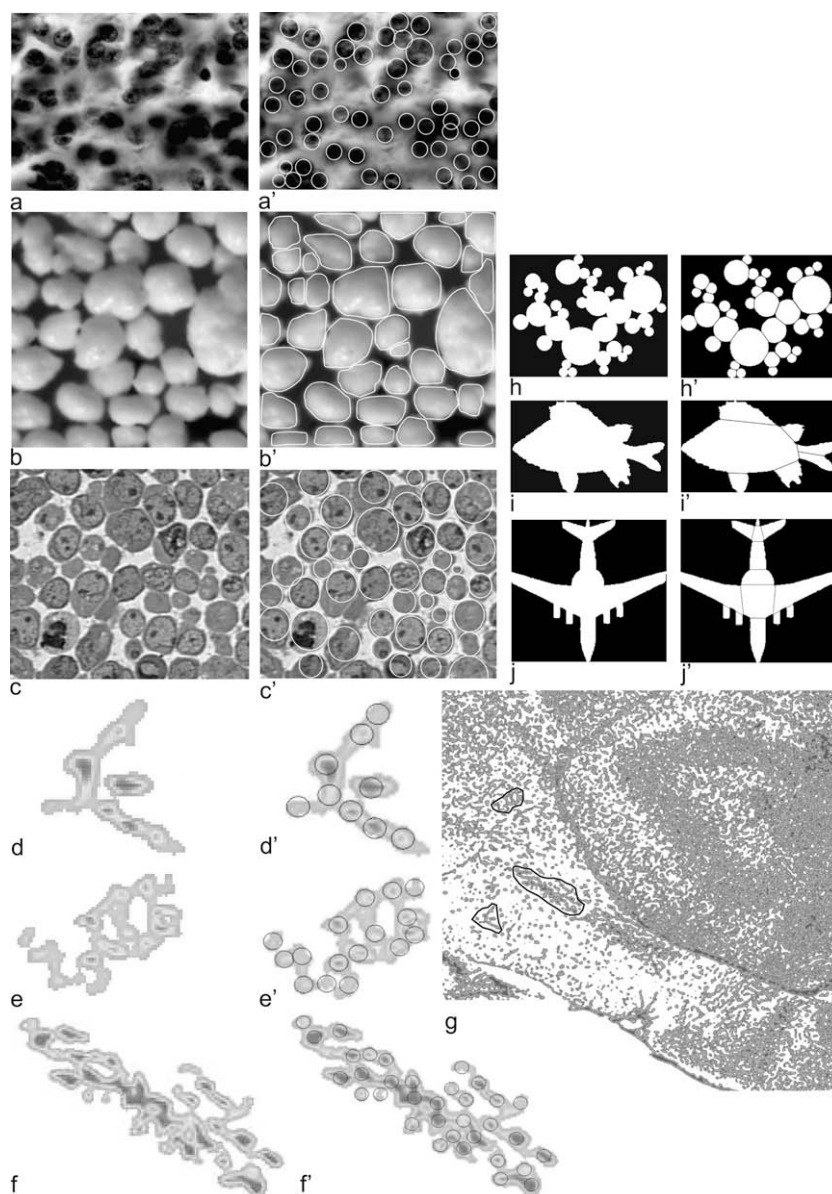


**Fig. 4.** A micrograph containing cell clusters of the dentate gyrus is shown in (a). (b), (c) and (h) are taken from [94]. With respect to object shape and positioning of objects in (b) and (c) these structures are comparable to cellular object (taken from [94]). (d–f) High-resolution scans of cells from a mouse brain. A part of the scan of a coronal mouse brain section is shown in (g) where the regions are marked by three black polygons. (i and j) are from the *Squid image database* (<http://www.ee.surrey.ac.uk/Research/VSSP/imagenet/demo.html>) used for shape description algorithms. However, the latter images were contributed originally by [57]. ([http://visual.ipan.sztaki.hu/corner/corner\\_click.html](http://visual.ipan.sztaki.hu/corner/corner_click.html)). The expected decompositions are shown on the right side of each original image. Letters without apostrophe designate the original images and those with an apostrophe the expected decompositions done by investigators.

In a further experiment the splitting results of WSD and MSD for large and small cell clusters of two high-resolution flat bed scanned histological sections of rat brain were compared (Fig. 8). The ROIs are located in regions with large cell densities like the substantia nigra, the hippocampus, the entorhinal region and the amygdala complex (Fig. 8a and b). Within the ROI images the largest and second largest connected region was determined. A rectangular cropping was performed. The resulting cropped regions are transferred to the gray-level images shown in Fig. 8c–u. After binarization the WSD and MSD were performed. The WSD result is marked with red lines and the MSD result with green lines. Those regions which were splitted by MSD but not by the WSD are marked with a green plus sign. In all cases this split paths of the MSD are fitting the local cell distribution. A green minus sign was put at those regions where the WSD performed a correct split but MSD do not put a split path (Fig. 8c–e, m, and o). Red minus signs (Fig. 8d, f, j, s, and t) were put

at regions where WSD yields an oversegmentation. In conclusion, the MSD does not generate oversegmentations. However, in some situations MSD tends to undersegmentations whereby the WSD shows numerous oversegmentations and undersegmentations.

To compare the similarity of MSD and WSD results with the EXD the rand index (RI) [117,118] and boundary displacement error (BDE) [31] was used. The RI is the ratio of the number of pairs of pixels having the compatible label relationship in MSD and EXD, respectively, WSD and EXD. A large RI means a good match of the algorithmic segmentation and the human generated expected segmentation (ground truth). The BDE evaluates segmentation quality in terms of the precision of the splitted region boundaries. It is based on a distance measure meaning that small values indicate a good match of the algorithmic segmentation and the ground truth. The MSD provides a mean RI of 0.75 with a standard error of mean (SEM) of 0.09. The WSD gives a mean RI of 0.61 with a stan-

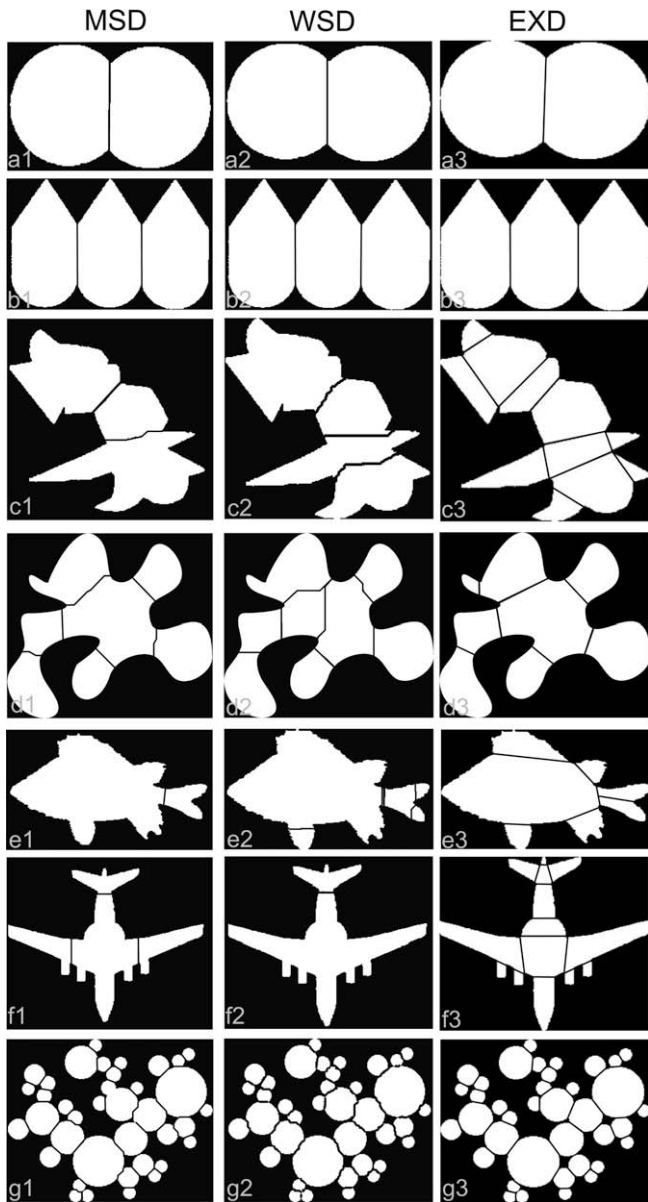


**Fig. 5.** Results of partitioning by morphological multiscale decomposition (MSD) in the first column (a1–g1), watershed decomposition (WSD) in the second column (a2–g2), and expected decomposition (EXD) in the third column (a3–g3). The latter was realized by an evaluator. Here, most images do not possess holes. In (b1), (c1), (e1) and (f1) the connected regions exhibit mixtures of corners and continuous concavities. The images (c1), (c2), (e1), (e2), (f1) and (f2) are not partitioned satisfying neither by (WSD) nor (MSD).

standard error of mean (SEM) of 0.1. With regard to RI the MSD splitting matches better with the ground truth than the WSD. This result coincides with the BDE where MSD splitting leads to 5.01 (SEM 1.5) and WSD provides a BDE of 5.99 (SEM 1.42).

#### 4. Discussion

The synthetic images were developed as bilevel images. The gray-level images in Fig. 7 were segmented by the method of [78]. The global segmentation strategy was applied because shading errors do not appear in flat bed scanned images and we have optimized microscopic illumination with regard to maximizing homogeneity. Therefore, shading corrections that effects local gray level distributions were not necessary and local adaptive thres-

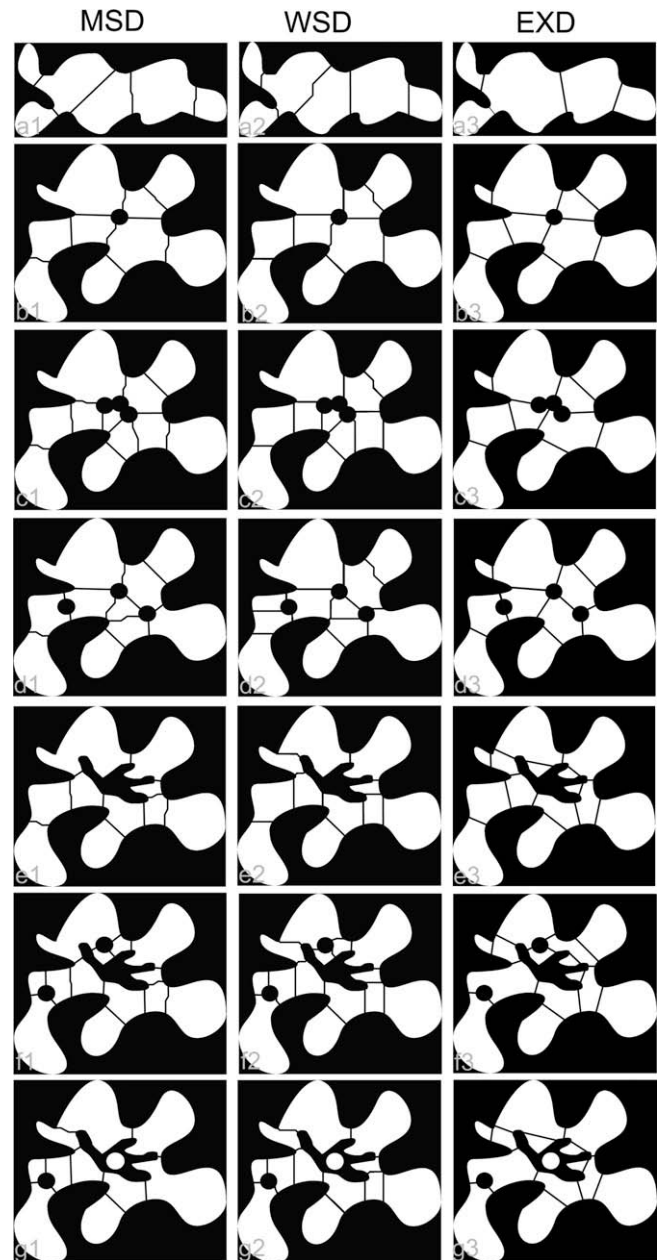


**Fig. 6.** Analog to the last figure results of partitioning by morphological scale decomposition (MSD) are presented in the first column, those of watershed decomposition (WSD) in the second column, and the expected decompositions (EXD) are shown in the third column. As mentioned earlier, the latter was realized by an evaluator. In contrast to the latter figure, most images do possess holes.

holding was avoided because it turns out to be complex if frame adaption is object size driven. The latter emerge to be problematic due to the high variability of cell cluster sizes which can be presented in multiple tiles of images if larger histological regions (image mosaics) are analyzed. Further global segmentations like mean-shift [33,17,18] and K-means [69,15,54] lead to similar segmentation results like the method of [78]. Preprocessing steps for noise removal either of the foreground or of the background turns out to be necessary to reduce oversegmentations. The size of the employed structuring elements for the opening and closing do not effect the structures of interest, i.e. different types of biological cells because these are considerably larger.

The testing of the MSD algorithm on the basis of a ground truth splitting (EXD) comprise problems if clusters are complex whereby

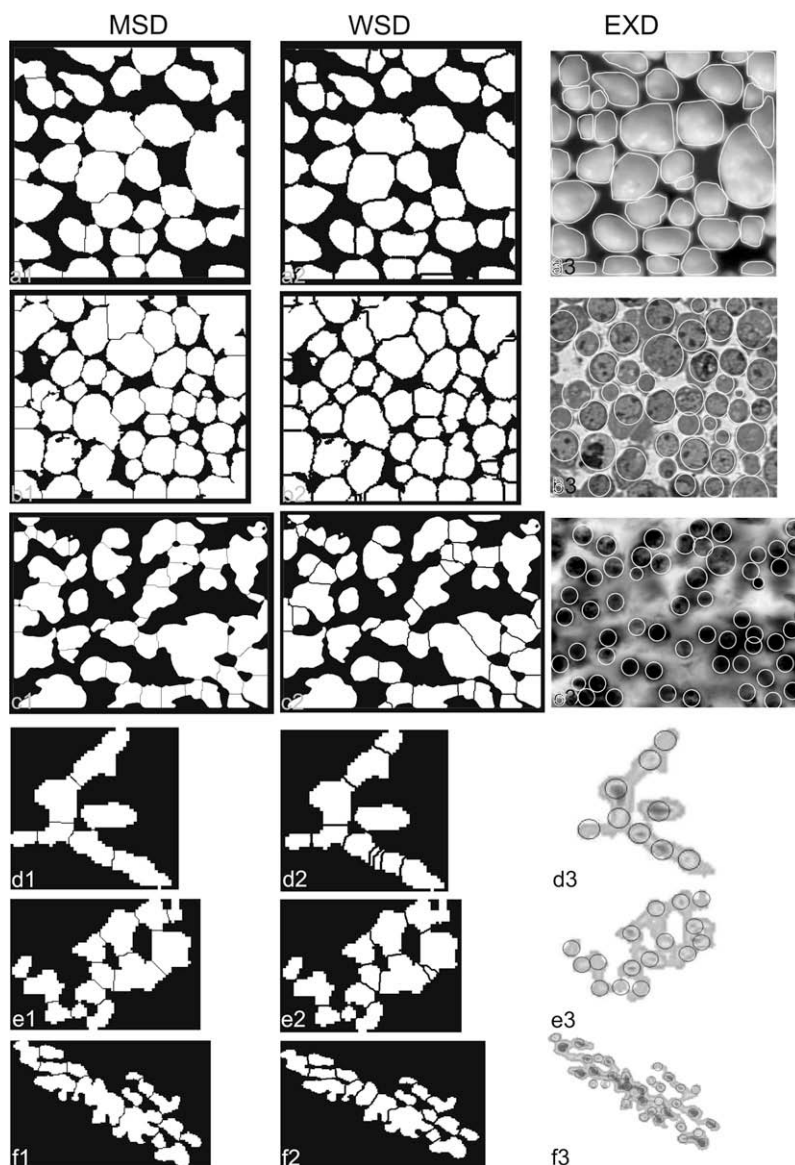


Fig. 7. In the first column the results of the MSD are shown, in the second those of the WSD and those of the EXD in the last column.

in simple synthetic images the ground truth of a splitting can be generated easily. Even if the test persons are urged to connect opposed concavities and holes having short distances to each other, providing convex shapes and minimizing the difference of the size of areas of the splitted parts the ground truth between persons may vary. However, in our experiments we do not found stronger variations of splittings like orthogonal split paths derived from different persons even in complex images.

As described by [70,71] ultimately eroded points determined by the maximal distance from all adjacent ultimate eroded points are centers of individual objects [106] that can be used for calculating separation lines between them. However, Metzler et al. pointed out that this entails that all objects have to be of similar size and objects must exhibit regular shapes. Hence, compact regions of different size cannot be decomposed correctly because the marker generation depends on size and scale.

The WSD [125,9,124,75,23,52] is modified, optimized to the specific object segmentation problem and applied by most investigators [125,9,124,63,75,23,20,122,2,52,27]. Since the WSD can be accessed easily because it is implemented in many software pack-

ages for image analysis, it prevailed for many separation problems. Obvious advantages of the WSD is the applicability to different kinds of preprocessed binary and gray-level and color images containing domains to be decomposed which vary within certain ranges in size. Eventually, WSD can be easily adapted to multidimensional partition problems [56].

However, this approach has limitations in regard to cell clusters composed of cells with large differences of cell areas, shapes and center-to-center distances that are smaller than the radius of the assembled objects [52]. Here, we observed problems in terms of holes within clusters of objects. If juxtaposed objects share larger overlapping regions WSD becomes less effective. When WSD is applied to irregularly shaped regions it causes unsatisfying splittings. We observed cap-like separations at large protrusions covering small areas. Another disadvantage are the inaccurate split paths which are situated around concavities, however, not passing exactly the concavities. Overall, WSD clearly exhibit obvious differences to the expected decompositions (EXD). With respect to decomposition problems of a larger class of planar domains WSD turns out to be inappropriate.

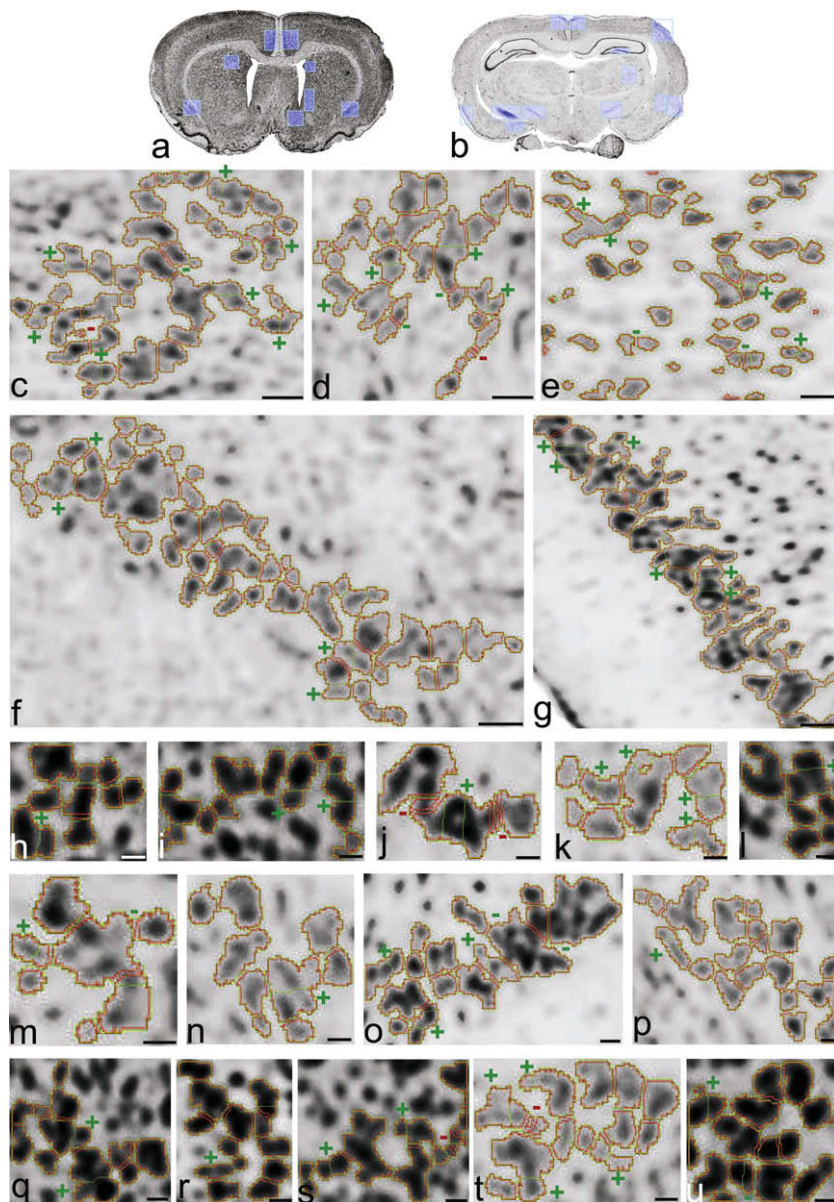


**Fig. 8.** Here, cell splitting of cell clusters that appear in high resolution scanned brain sections of the rat brain are of primary interest. In (a) and (b) the two sections of a rat brain are shown in which regions of interest were cropped and highlighted by blue rectangular regions. All sample images (c)–(u) are taken from the latter regions. Red lines are generated by the WSD while green lines are produced by the MSD. Those cell regions which were splitted in addition by MSD by contrast to WSD are marked by a green plus sign. Cell regions within clusters which were separated by WSD but not by MSD are marked by a green minus sign: (c)–(e), (m), (o), and (u). Oversegmentations of the WSD are marked by a red minus sign: (f), (j), (s), and (t). Scale bars: (c)–(g) 50  $\mu\text{m}$ , (h)–(u) 20  $\mu\text{m}$ .

The two-stage multiscale approach avoids the drawbacks due to irregular shaped regions, large and long protrusions covering small areas and inaccurate positioning of split paths mentioned before. These disadvantages of the watershed technique result mainly from its single-scale nature. The generation of a morphological scale space, filtering of false markers, and their stepwise reconstruction is independent of the object's size and additionally improve results.

The MSD can be applied successfully to object compositions with strong discontinuities or corners. Especially, shapes that are elongated or where objects are clustered in a chain-like manner can be partitioned efficiently by the MSD. The result of the MSD algorithm is strongly dependent on the size and shape of the structuring element  $\sigma$ , however, this is the exclusive parameter if we do not have fitted the number of scales  $k$  to the size of domains to be decomposed. This seems adequate, since size and shape of cell clusters in the CNS may vary considerably.

We intend to solve partitions of strongly clustered cells of different size and shape which may come up to huge and highly complex clusters like that shown in Fig. 4g whereas the WSD may not be suitable in terms of reliability. With regard to the size of cell clusters the complexity of the MSD algorithm was determined. The required time to perform a splitting by the MSD is a quadratic function of the number of foreground pixels  $\#(X^1(I))$ , whereas the quadratic coefficient  $a$  is a very small number ( $a \leq 1 \times 10^{-6}$ ). Currently we are implementing the parallelization of basic morphologic functions and first results show a promising speedup especially for large images on multi-processor machines. Therefore, the computational cost is a problem that can be solved since it turns out that the new MSD approach offers some important advantages with regard to partitioning of objects covering features of:

- convex and concave corners,
- convex and concave curves,

- geometric hierarchies of concavities and convexities, and
- domains with holes within clusters of objects.

An important feature of the MSD is its reliability with regard to similar split paths if holes are added to the same cluster of objects what speaks in favor for robustness. It was shown that objects with strong discontinuities like the example of the binary plane (Fig. 5f3) and the binary fish silhouette (Fig. 5e3) result in partitions that are rather similar like those derived from EXD. A disadvantage seems to be the partition of small protrusions with regard to the area of the appropriate domain Fig. 5e1, however, in most cases such small protrusions are not individual cells rather non-cellular material of the neuropil, appendages of cells or artifacts. Strong corner-like protrusions in combination with small curve-like concavities like those in Fig. 5c1 and f1 yield to few partitions. The numerous oversegmentations of the WSD regardless smoothing the distance transform are not observed in the MSD results. This phenomenon was found in several different images of different cluster sizes emphasizing again the robustness of the MSD. Moreover, the MSD determined split paths that were not found by the classical WSD approach. In the majority of these cases the partitions are in line with contour concavities which are characteristic for attached cells. Therefore, the correctness of MSD turns out to be superior with regard to WSD.

It is now clear that, in addition to strong overlaps of domains containing multiple holes (Fig. 7a1–e1) such subregions of a connected component can be integrated into meaningful split paths. This observation suggests, that compared to other studies the MSD approach has some principal advantages concerning partition of clustered regions with emerging complexity. At this point of time, however, it has not been possible to identify clearly separated cells in huge clusters of several thousands of cells each composed of a few pixels which are derived from high-resolution flat bed scanning. Therefore, this issue is considered currently by developing pre-partitioning steps and parallelized algorithms. We have presented experimental data that the MSD approach turns out to be a suitable splitting technique, while not definitive, will provide a useful perspective for future investigations of decomposing highly complex aggregations of biological cells.

## Acknowledgments

The authors gratefully acknowledge the encouragement and valuable criticism of Prof. Manfred Tasche of the Institute of Mathematics and Prof. Andreas Wree of the Institute of Anatomy of the University of Rostock.

## References

- [1] P. Adiga, B. Chaudhuri, K. Rodenacker, K., Semiautomatic segmentation of tissue cells from confocal microscope images, in: *ICPR'96*, pp. 494–497.
- [2] H. Ancin, T.E. Dufresne, G.M. Ridder, J.N. Turner, B. Roysam, An improved watershed algorithm for counting objects in noisy, anisotropic 3D biological images, in: *ICIP '95: Proceedings of the 1995 International Conference on Image Processing*, vol. 3, IEEE Computer Society, Washington, DC, USA, 1995, p. 3172.
- [3] H. Ancin, B. Roysam, T. Dufresne, M. Chestnut, G. Ridder, D. Szarowski, J. Turner, Advances in automated 3-D image analyses of cell populations imaged by confocal microscopy, *Cytometry* 25 (1996) 221–234.
- [4] C. Arcelli, L. Serino, From discs to parts of visual form, *Image Vis. Comp.* 15 (1997) 1–10.
- [5] F. Attneave, Some informational aspects of visual perception, *Psychol. Rev.* 61 (1954) 183–193.
- [6] P. Bamford, P. Jackway, B. Lovell, Progress in the robust automated segmentation of real cell images, *SPIE* 3747 (1999) 34–56.
- [7] E. Barenholtz, E. Cohen, J. Feldman, M. Singh, Detection of change in shape: an advantage for concavities, *Cognition* 89 (2003) 1–9.
- [8] E. Bengtsson, Computerized cell image analysis: past present, and future, *LNCS* 2749 (2003) 395–407.
- [9] E. Bengtsson, C. Wählby, J. Lindblad, Robust cell image segmentation methods, *Pattern Recogn. Image Anal.* 14 (2004) 157–167.
- [10] M. Bertamini, C. Croucher, The shape of holes, *Cognition* 87 (2003) 33–54.
- [11] G.-A. Bilodeau, Part segmentation of objects in real images, *Pattern Recogn.* 35 (2002) 2913–2926.
- [12] M. Bilodeau, F. Meyer, M. Schmitt, *Lecture Notes in Statistics: Space, Structure and Randomness*, Springer-Verlag, New York, 2006, vol. 183.
- [13] U. Braga-Neto, Multiscale connected operators, *J. Math. Image Vis.* 22 (2005) 199–216.
- [14] P. Burt, E. Adelson, The Laplacian pyramid as compact image code, *IEEE Trans. Commun.* 31 (1983) 532–540.
- [15] C. Chen, J. Luo, K. Parker, Image segmentation via adaptive K-mean clustering and knowledge-based morphological operations with biomedical applications, *IEEE Trans. Image Process.* 7 (1998) 1673–1683.
- [16] W. Clocksin, Automatic segmentation of overlapping nuclei with high background variation using robust estimation and flexible contour models, *ICIAAP* 1 (2003) 682–687.
- [17] D. Comaniciu, P. Meer, Mean shift analysis and applications, in: *ICCV '99: Proceedings of the International Conference on Computer Vision*, vol. 2, IEEE Computer Society, Washington, DC, USA, 1999, pp. 1197–1203.
- [18] D. Comaniciu, P. Meer, Mean shift: a robust approach toward feature space analysis, *IEEE Trans. Pattern Anal. Mach. Intell.* 24 (2002) 603–619.
- [19] L. Costa, R.M. Cesar, *Shape Analysis and Classification*, CRC Press, Boca Raton, 2001.
- [20] J. Costa, D. Mascarenhas, L. Marcio, M. de Andrade Netto, Cell nuclei segmentation in noisy images using morphological watersheds, *SPIE* 3164 (1997) 314–324.
- [21] J. Crespo, V. Maojo, New results on the theory of morphological filters by reconstruction, *Pattern Recogn.* 31 (1998) 419–429.
- [22] T. Cronin, Visualizing concave and convex partitioning of 2D contours, *Pattern Recogn. Lett.* 24 (2003) 429–443.
- [23] Y. Cui, N. Zhou, Blob analysis using watershed transformation, *LNAI* 1821 (2000) 482–491.
- [24] E. Dejnozkova, P. Dokladal, Modelling of overlapping circular objects based on level set approach, *LNCS* 3211 (2004) 416–423.
- [25] A. Desolneux, L. Moisan, J.-M. Morel, *From Gestalt Theory to Image Analysis*, Springer, New York, 2008.
- [26] E. Dougherty, *Mathematical Morphology in Image Processing*, Marcel Dekker, New York, Basel, Hong Kong, 1993.
- [27] A. Dow, S. Shafer, A. Waggoner, Morphological segmentation of multi-probe fluorescence images for immunophenotyping in melanoma tissue sections, *SPIE* 2055 (1993) 487–498.
- [28] A. Elmoataz, S. Schupp, R. Clouard, P. Herlin, D. Bloyet, Using active contours and mathematical morphology tools for quantification of immunohistochemical images, *Signal Process.* 71 (1998) 215–226.
- [29] J. Feldman, M. Singh, Information along contours and objects, *Psychol. Rev.* 112 (2005) 243–252.
- [30] D. Foran, R. Berg, A method for quantitative image assessment based on redundant feature measurements and statistical reasoning, *Comp. Methods Prog. Biomed.* 45 (1994) 291–305.
- [31] J. Freixenet, X. Mu n, D. Raba, J. Martí, X. Cufí, Yet another survey on image segmentation: region and boundary information integration, *LNCS* 2352 (2002) 408–422.
- [32] K. Fukunaga, *Introduction to Statistical Pattern Recognition*, Academic Press, New York, 1990.
- [33] F. Gallyas, M. Hsu, G. Buzsaki, Four modified silver methods for thick sections of formaldehyde-fixed mammalian central nervous tissue: 'dark' neurons, perikarya of all neurons, microglial cells and capillaries, *J. Neurosci. Methods* 50 (1993) 159–164.
- [34] J.M. Geusebroek, A.W.M. Smeulders, F. Cornelissen, Segmentation of cell clusters by nearest neighbour graphs, in: *ASCI'97, Proceedings of the Third Annual Conference of the Advanced School for Computing and Imaging*, 1997, pp. 248–252.
- [35] J.M. Geusebroek, A.W.M. Smeulders, F. Cornelissen, H. Geerts, Segmentation of tissue architecture by distance graph matching, *Cytometry* 35 (1999) 12–22.
- [36] E.E. Gose, W.H. Rose, W.E. Barnes, E. Kaplan, J.S. Arnold, Decomposition of image sequences of overlapping homogeneous transparent radiating objects, in: *International Conference of pattern Recognition (ICPR80)*, 1980, pp. 971–973.
- [37] J. Goutsias, H. Heijmans, Multiresolution signal decomposition schemes. Part 1: Linear and morphological pyramids, *IEEE Trans. Image Process.* 9 (2000) 1862–1876.
- [38] S. Grinaker, Edge based segmentation and texture separation in: *International Conference of pattern Recognition (ICPR80)*, 1980, pp. 554–557.
- [39] R. Haralick, L. Shapiro, Image segmentation techniques, *CVGIP* 29 (1985) 100–132.
- [40] H. Heijmans, *Shape in Picture: Mathematical Description of Shape in Grey-level Images. Mathematical Morphology as a Tool for Shape Description*, Springer, Berlin, 1994.
- [41] H. Heijmans, R. van den Boomgaard, Algebraic framework for linear and morphological scale-spaces, *J. Math. Image Vis.* 13 (2002) 269–301.
- [42] V. Hodge, G. Hollier, J. Eakins, J. Austin, Eliciting perceptual ground truth for image segmentation, in: *CIVR06*, 2006, pp. 320–329.
- [43] D. Hoffman, M. Singh, Saliency of visual parts, *Cognition* 63 (1997) 29–78.

- [44] P. Jackway, Morphological Scale-space with Application to Three-dimensional Object Recognition. Ph.D. Thesis, Queensland University of Technology, Brisbane, 1994.
- [45] P. Jackway, Gradient watersheds in morphological scale-space, *IEEE Image Proc.* 5 (1996) 913–921.
- [46] C. Jung, Multiscale Image Segmentation using Wavelets and Watersheds, in: *SIBGRAPI'03*, 2003, pp. 278–284.
- [47] S. Kumar, H.O. S, S. Ranganath, T. Ong, F. Chew, A rule-based approach for robust clump splitting, *Pattern Recogn.* 39 (2006) 1088–1098.
- [48] V. Lakshmanan, V. DeBrunner, R. Rabin, Nested partitions using texture segmentation, *SSIAI 00* (2002) 0153.
- [49] V. Leavers, Shape Detection in Computer Vision using the Hough Transform, Springer, Berlin, 1992.
- [50] T. Lee, M. Atkins, A new approach to measure border irregularity for melanocytic lesions, *SPIE* 3979 (2000) 668–675.
- [51] Y.-K. Lee, J.-H. Kim, An efficient morphological segmentation for significantly overlapped particles, *SPIE* 2424 (1995) 349–357.
- [52] T. Lee, M. Atkins, Z.-N. Li, Indentation and protrusion detection and its applications, *LNCS* 2106 (2001) 335–343.
- [53] A. Likas, N. Vlassis, J. Verbeek, The global k-means clustering algorithm, *Pattern Recogn.* 36 (2003) 451–461.
- [54] J. Lindblad, C. Wählby, E. Bengtsson, A. Zaltsman, Image analysis for automatic segmentation of cytoplasm and classification of Rac1 activation, *Cytometry* 57 (2004) 22–33.
- [55] G. Lin, U. Adiga, K. Olson, J. Guzowski, C. Barnes, B. Roysam, A hybrid 3D watershed algorithm incorporating gradient cues and object models for automatic segmentation of nuclei in confocal image stacks, *Cytometry* 56 (2003) 23–36.
- [56] G. Lin, M. Chawia, K. Olson, J. Guzowski, C. Barnes, B. Roysam, Hierarchical, model-based merging of multiple fragments for improved three-dimensional segmentation of nuclei, *Cytometry* 63 (2004) 20–33.
- [57] L. Liu, S. Sclaroff, Region segmentation via deformable model-guided split and merge, *ICCV* 1 (2001) 98–104.
- [58] H.-C. Liu, M. Srinath, Corner detection from chain-code, *Pattern Recogn.* 21 (1990) 51–68.
- [59] Z. Liu, D. Jacobs, R. Basri, The role of convexity in perceptual completion: beyond good continuation, *Vis. Res.* 39 (1999) 4244–4257.
- [60] T. Liu, G. Li, J. Nie, A. Tarokh, X. Zhou, L. Guo, J. Malicki, W. Xia, S. Wong, An automated method for cell detection in zebrafish, *Neuroinformatics* 6 (2008) 5–21.
- [61] S. Loncaric, A survey of shape analysis techniques, *Pattern Recogn.* 31 (1998) 983–1001.
- [62] C. Loukas, G. Wilson, B. Vojnovic, Automated segmentation of cancer cell nuclei in complex tissue sections, *SPIE* 4158 (2001) 188–198.
- [63] R. Malladi, *Geometric Methods in Bio-medical Image Processing*, Springer, Berlin, 2001.
- [64] N. Malpica, C.O. de Solorzano, J. Vaquero, A. Santos, I. Vallcorba, J.M. Garcia-Sagredo, F. del Pozo, Applying watershed algorithms to the segmentation of clustered nuclei, *Cytometry* 28 (1997) 289–297.
- [65] P. Maragos, Pattern spectrum and multiscale shape representation, *IEEE Trans. PAMI* 11 (1989) 701–716.
- [66] P. Maragos, R. Schaffer, Morphological filters. Part II: Their relation to median, order-statistic, and stack filters, *IEEE Trans. Acoust. Speech Signal Process.* 35 (1987) 1170–1184.
- [67] M. Marji, P. Siy, Polygonal representation of digital planar curves through dominant point detection—a nonparametric algorithm, *Pattern Recogn.* 37 (2004) 2113–2130.
- [68] J. McQueen, Some Methods for Classification and Analysis of Multivariate Observations, in: *Proceedings of the Fifth Berkeley Symposium on Mathematical Statistics and Probability*, vol. 1, 1967, pp. 281–297.
- [69] V. Metzler, T. Lehmann, T. Aach, Morphological multiscale shape analysis of light micrographs, *SPIE* 3961 (2000) 227–238.
- [70] V. Metzler, T. Lehmann, H. Bienert, K. Mottaghy, K. Spitzer, Scale-independent shape analysis for quantitative cytology using mathematical morphology, *Comp. Biol. Med.* 30 (2000) 135–151.
- [71] F. Meyer, S. Beucher, Morphological segmentation, *J. Vis. Commun. Image Rep.* 1 (1990) 21–46.
- [72] J. Modersitzki, *Numerical Methods for Image Registration*, Oxford University Press, Oxford, 2004.
- [73] A. Nedzved, S. Ablameyko, I. Pitas, Morphological segmentation of histology cell images, *ICPR* 1 (2000) 1500–1504.
- [74] B. Nilsson, A. Heyden, Segmentation of dense leukocyte clusters, in: *Proc. MMBIA*, vol. 1, pp. 221–227.
- [75] J. Norman, F. Phillips, H. Ross, Information concentration along the boundary contours of naturally shaped solid objects, *Perception* 30 (2001) 1285–1294.
- [76] C. Orbert, E. Bengtsson, B. Nordin, Watershed segmentation of binary images using distance transformations, *SPIE* 1902 (1992) 159–170.
- [77] N. Otsu, A threshold selection method from gray level histograms, *IEEE Trans. Syst. Man Cyb.* 9 (1979) 62–66.
- [78] N. Pal, S. Pal, A review on image segmentation techniques, *Pattern Recogn.* 26 (1993) 1277–1294.
- [79] T. Pavlidis, S. Horowitz, Segmentation of plane curves, *IEEE Trans. Comput.* 23 (1974) 860–870.
- [80] D. Pham, Robust fuzzy segmentation of magnetic resonance images, in: *Proc 14th IEEE Symp Comp-Based Med Syst (CBMS2001)*, 2001, pp. 127–131.
- [81] D. Pham, J. Prince, An adaptive fuzzy C-means algorithm for image segmentation in the presence of intensity inhomogeneities, *Pattern Recogn. Lett.* 20 (1999) 57–68.
- [82] D. Pham, J. Prince, An adaptive fuzzy segmentation algorithm for three-dimensional magnetic resonance images, *LNCS* 1613 (1999) 140–153.
- [83] D. Pham, J. Prince, Adaptive fuzzy segmentation of magnetic resonance images, *IEEE Trans. Med. Imaging* 18 (1999) 737–752.
- [84] G.G. Pieroni, M.F. Costabile, G. Guerra, Decomposition of shape boundaries in a problem of map sequence analysis, in: *A comparison of some segmentation algorithms for cytology*, 1980, pp. 618–623.
- [85] S. Pizer, D. Fritsch, P. Yushkevich, V. Johnson, E. Chaney, Segmentation registration and measurement of shape variation via image object shape, *IEEE Trans. Med. Imaging* 18 (1999) 851–865.
- [86] S. Portet, J. Vassy, M. Beil, G. Millot, A. Hebbache, J. Rigault, D. Schoevaert, Quantitative analysis of cytokeratin network topology in the MCG7 cell line, *Cytometry* 35 (1999) 203–213.
- [87] J. Reinhardt, W. Higgins, Comparison between the morphological skeleton and morphological shape decomposition, *IEEE Trans. PAMI* 18 (1996) 951–957.
- [88] H. Resnikoff, *The Illusion of Reality: Topics in Information Science*, Springer-Verlag, New York, 1985.
- [89] S. Rist, Ein Ansatz zur Klassifizierung biologischer Neuronen mittels künstlicher neuronaler Netze. Technical report, Institute of Mathematics, University of Lübeck, 1999.
- [90] K. Rodenacker, E. Bengtsson, A feature set for cytometry on digitized microscopic images, *Anal. Cell Path.* 25 (2003) 1–36.
- [91] J. Roerdink, A. Meijster, The watershed transform: definitions, algorithms and parallelization strategies, *Fund. Inform.* 41 (2001) 187–228.
- [92] P. Rosin, Shape partitioning by convexity, *IEEE Trans. Syst. Man Cyb. A* 30 (2000) 202–210.
- [93] J. Rowinski, C. Souchier, J. Czyba, M. Pages, R. Fages, J. Laurent, T. Greenland, Morphometric studies of cell nuclei by means of image analysis and computer data processing, *Gegenbaurs Morphol. Jahrb.* 126 (1980) 253–263.
- [94] J. Russ, *The Image Processing Handbook*, CRC Press, Boca Raton, 2002.
- [95] P. Sahoo, S. Soltani, A. Wong, Y. Chen, A survey of thresholding techniques, *CVGIP* 41 (1988) 233–260.
- [96] A. Salden, Dynamic scale-space paradigms versus mathematical morphology, *SPIE* 3716 (1999) 155–166.
- [97] P. Salembier, M. Kunt, Size-sensitive multiresolution decomposition of images with rank-order based filters, *Signal Process.* 27 (1992) 205–241.
- [98] M. Salotti, An efficient algorithm for the optimal polygonal approximation of digitized curves, *Pattern Recogn. Lett.* 22 (2001) 215–221.
- [99] O. Schmitt, R. Eggers, Systematic investigations of the contrast results of histochemical stainings of neurons and glial cells in the human brain by means of image analysis, *Micron* 28 (1997) 197–215.
- [100] O. Schmitt, R. Eggers, Flat-bed scanning as a tool for quantitative neuroimaging, *J. Microsc.* 196 (1999) 337–346.
- [101] O. Schmitt, R. Eggers, J. Modersitzki, Videomicroscopy, image processing, and analysis of whole histologic sections of the human brain, *Microsc. Res. Technol.* 66 (2005) 203–218.
- [102] S. Schüpp, A. Elmoataz, M.-J. Fadili, D. Bloyet, Fast statistical level sets image segmentation for biomedical applications, *LNCS* 2106 (2001) 380–388.
- [103] S. Sclaroff, L. Liu, Deformable shape detection and description via model-based region grouping, *IEEE Trans. Pattern Mach. Intell.* 23 (2001) 475–489.
- [104] S. Serpico, G. Vernazza, S. Dellepiane, Merging of different segmentation techniques for self image recognition, *SPIE* 1027 (1988) 208–213.
- [105] J. Serra, *Image Analysis and Mathematical Morphology*, vol. 1, Academic Press, London, 1993.
- [106] J. Shah, Segmentation of Shapes, *LNCS* 2106 (2001) 236–244.
- [107] C. Shannon, A mathematical theory of communication, *Bell Syst. Tech. J.* 27 (1948) 379–423.
- [108] K. Siddiqi, K. Tresness, B. Kimia, Parts of visual form: psychophysical aspects, *Perception* 25 (1996) 399–424.
- [109] P. Soille, *Morphological image analysis, Principles and applications*, Springer, Berlin, 2006.
- [110] O. Stephansson, W. Wang, S. Dahlhielm, Automatic image processing of aggregates, in: *ISRM Symposium: Eurock'92*, 1992, pp. 31–35.
- [111] M. Szegin, B. Sankur, Survey over image thresholding techniques and quantitative performance evaluation, *J. Elect. Imaging* 13 (2004) 146–165.
- [112] H. Talbot, B. Appleton, Elliptical distance transforms and the object splitting problem, in: *Proceedings of ISMM2002*, 2002, pp. 229–240.
- [113] D. Thompson, H. Bartels, J. Haddad, P. Bartels, Scene segmentation in a machine vision system for histopathology, *SPIE* 1206 (1990) 40–47.
- [114] K. Thórisson, Simulated perceptual grouping: an application to human-computer interaction, in: *Proceedings of the 16th Annual Conference of Cognitive Science Society*, Atlanta, GA, 1994, pp. 876–881.
- [115] M. Tánase, R. Veltkamp, Polygon decomposition based on the straight line skeleton, *SoCG* 1 (2003) 58–67.
- [116] R. Unnikrishnan, M. Hebert, Measures of similarity, in: *Seventh IEEE workshop on applications of computer vision*, 2005, pp. 394–400.
- [117] R. Unnikrishnan, C. Pantofaru, M. Hebert, Toward objective evaluation of image segmentation algorithms, *IEEE Trans. PAMI* 29 (2007) 929–944.
- [118] C. Vachier, F. Meyer, The viscous watershed transform, *J. Math. Imag. Vis.* 22 (2005) 251–267.

- [119] R. van den Boomgaard, L. Dorst, Gaussian Scale-space Theory. The Morphological Equivalent of Gaussian Scale Space, Kluwer Academic Publishers, Dordrecht, 1996. pp. 203–220.
- [120] R. van den Boomgaard, A. Smeulders, The morphological structure of images: the differential equations of morphological scale-space, *IEEE Trans. Pattern Anal. Mach. Intell.* 16 (1994) 1101–1113.
- [121] P. van Ham, C. de Hauwer, R. Kiss, Dynamic behaviour analysis of in vitro cancerous cells by means of an automatic image processing device, *SPIE* 2710 (1996) 967–978.
- [122] L. Vincent, P. Soille, Watersheds in digital spaces: an efficient algorithm based on immersion simulations, *IEEE Trans. Pattern Anal. Mach. Intell.* 13 (1991) 583–597.
- [123] C. Wahlby, E. Bengtsson, Segmentation of cell nuclei in tissue by combining seeded watersheds with gradient information, *LNCS* 2749 (2003) 408–414.
- [124] C. Wahlby, I.-M. Sintorn, F. Erlandsson, G. Borgefors, E. Bengtsson, Combining intensity, edge and shape information for 2D and 3D segmentation of cell nuclei in tissue sections, *J. Microsc.* 215 (2004) 67–76.
- [125] W. Wang, H. Song, Cell cluster image segmentation on form analysis, *ICNC* 4 (2007) 833–836.
- [126] Q. Wei, C. Reme, P. Stucki, Advanced image processing and modeling system for the analysis of cell micrographs in morphology, *SPIE* 1905 (1993) 175–185.
- [127] J. Weszka, A survey of threshold selection techniques, *CGIP* 7 (1978) 259–265.
- [128] A. Witkin, *Image Understanding. Scale Space Filtering: A New Approach to Multi-Scale Description*, Ablex, Norwood, NY, 1984. pp. 79–95.
- [129] H.-S. Wu, J. Barba, J. Gil, A parametric fitting algorithm for segmentation of cell images, *IEEE Trans. Biomed. Eng.* 45 (1998) 400–407.
- [130] C. Xiaohua, Y. Chang, Application of some valid methods in cell segmentation, *SPIE* 4550 (2001) 340–344.
- [131] J. Xu, Morphological decomposition of 2-D binary shapes into conditionally maximal convex polygons, *Pattern Recogn.* 29 (1996) 1075–1104.
- [132] F. Yang, T. Jiang, Cell image segmentation with kernel-based dynamic clustering and an ellipsoidal cell shape model, *J. Biomed. Inform.* 34 (2001) 67–73.
- [133] Q. Yang, B. Parvin, Harmonic cut and regularized centroid transform for localization of subcellular structures, *IEEE Trans. Biomed. Eng.* 50 (2003) 469–475.
- [134] T. Yeo, X. Jin, S. Ong, S. Jayasooriah, R. Sinniah, Clump splitting through concavity analysis, *Pattern Recogn. Lett.* 15 (1994) 1013–1018.
- [135] Z. Yu, C. Bajaj, Image segmentation using gradient vector diffusion and region merging, in: *ICPR02, 2002*, pp. II: 941–944.
- [136] Z. Yu, C. Bajaj, Normalized gradient vector diffusion and image segmentation, in: *ECCV02, 2002*, pp. III: 517–530.
- [137] Y. Zhang, Evaluation and comparison of different segmentation algorithms, *Pattern Recogn. Lett.* 18 (1997) 963–974.
- [138] D. Zhang, G. Lu, Review of shape representation and description techniques, *Pattern Recogn.* 37 (2004) 1–19.
- [139] C. Zimmer, E. Labruière, V. Meas-Yedid, N. Guillén, J.-C. Olivo-Marin, Segmentation and tracking of migrating cells in videomicroscopy with parametric active contours: a tool for cell-based drug testing, *IEEE Trans. Med. Imaging* 21 (2002) 1212–1221.